Crystal Structure of Monofunctional Histidinol Phosphate Phosphatase from *Thermus thermophilus* HB8‡

Rie Omi,[§,||] Masaru Goto,[§,||] Ikuko Miyahara,[§,||] Miho Manzoku,[§] Akio Ebihara,[§] and Ken Hirotsu*[,§,||]

RIKEN Spring-8 Center, Harima Institute, 1-1-1 Kouto, Sayo, Hyogo 679-5148, Japan, and Department of Chemistry, Graduate School of Science, Osaka City University, Osaka 558-8585, Japan

Received June 18, 2007; Revised Manuscript Received August 14, 2007

ABSTRACT: Monofunctional histidinol phosphate phosphatase from *Thermus thermophilus* HB8, which catalyzes the dephosphorylation of L-histidinol phosphate, belongs to the PHP family, together with the PHP domain of bacterial DNA polymerase III and family X DNA polymerase. We have determined the structures of the complex with a sulfate ion, the complex with a phosphate ion, and the unliganded form at 1.6, 2.1, and 1.8 Å resolution, respectively. The enzyme exists as a tetramer, and the subunit consists of a distorted $(\beta\alpha)_7$ barrel with one linker and one C-terminal tail. Three metal sites located on the C-terminal side of the barrel are occupied by Fe1, Fe2, and Zn ions, respectively, forming a trinuclear metal center liganded by seven histidines, one aspartate, one glutamate, and one hydroxide with two Fe ions bridged by the hydroxide. In the complexes, the sulfate or phosphate ion is coordinated to three metal ions, resulting in octahedral, trigonal bipyramidal, and tetrahedral geometries around the Fe1, Fe2, and Zn ions, respectively. The ligand residues are derived from the four motifs that characterize the PHP family and from two motifs conserved in histidinol phosphate phosphatases. The $(\beta\alpha)_7$ barrel and the metal cluster are closely related in nature and architecture to the $(\beta\alpha)_8$ barrel and the mononuclear or dinuclear metal center in the amidohydrolase superfamily, respectively. The coordination behavior of the phosphate ion toward the metal center supports the mechanism in which the bridging hydroxide makes a direct attack on the substrate phosphate tridentately bound to the two Fe ions and Zn ion to hydrolyze the phosphoester bond.

Histidinol phosphate phosphatase (HisPPase),[1] step of histidine biosynthesis catalyzes the dephosphorylation of L-histidinol phosphate to give phosphate ion and histidinol, which is converted to histidine by histidinol dehydrogenase (*1*). The HisPPases are classified into the *Escherichia coli* and *Bacillus subtilis* types (*2*). The former is a bifunctional enzyme in which the N-terminal domain has HisPPase activity and the C-terminal domain has imidazole glycerol phosphate dehydratase activity. The enzyme belongs to the DDDD superfamily, named after the presence of the four invariant aspartate residues (*3*). Nonspecific acid phosphatase, phosphoglycolate phosphatase, phosphoserine phosphatase, and trehalose-6-phosphatase belong to the DDDD superfamily. The latter is a monofunctional enzyme with HisPPase activity. This enzyme is a member of the PHP family named after polymerase and HisPPase, the catalytic site of which has four motifs with conserved histidine residues. The PHP family includes the α-subunit of bacterial DNA polymerase III and family X DNA polymerases in addition to HisPPase. (*4*). Recently, the crystal structures of four proteins belonging to the PHP family were reported to have a distorted $(\beta\alpha)_7$ barrel fold. Hypothetical protein YcdX from *E. coli* (*5*) and the PHP domain of DNA polymerase III from *Thermus aquaticus* (*6*) possess a trinuclear metal site on the C-terminal side of the barrel. *Thermotoga maritima* TM0559 (PDB code 2ANU) is predicted to be a metal-dependent phosphoesterase with a tetranuclear metal site. Ribonuclease P protein Ph1877p, which is an essential component of *Pyrococcus horikoshii* ribonuclease P, has no metal site on the C-terminal side of the barrel (*7*).

The PHP domain (Pfam accession number PF02811) is found in more than 1500 different proteins and is present in organisms ranging from archaea and bacteria to fungi. The conserved residues of the PHP family are similar to those in a metal-dependent amidohydrolase superfamily (*4*). The amidohydrolase superfamily includes adenine and cytosine deaminases, aminocyclase, dihydroorotase, hydantoinase, urease, and phosphotriesterase, which are primarily involved in nucleotide metabolism (*8*, *9*). These enzymes have a common distorted $(\beta/\alpha)_8$ barrel, and its C-terminal side bears a metal binding site where a metal-activated water molecule acts as a nucleophile for hydrolysis of the substrate (*9*). The metal binding site carries the conserved residues, four histidines and one aspartate.

HisPPase from *Thermus thermophilus* HB8 (tHisPPase), belonging to the PHP family, was identified during the gene

‡ The atomic coordinates and structure factors for the sulfate complex, phosphate complex, and unliganded form have been deposited in the RCSB Protein Data Bank as entries 2YX0, 2YZ5, and 2Z4G, respectively.

* To whom correspondence should be addressed: tel +81-791-58-2891; fax +81-791-58-2892; e-mail hirotsu@spring8.or.jp.

§ RIKEN Spring-8 Center.

|| Osaka City University.

[1] Abbreviations: HisPPase, histidinol phosphate phosphatase; tHisPPase, HisPPase from *Thermus thermophilus* HB8; NAGPase, N-acetylglucosamine-6-phosphate deacetylase.

10.1021/bi701204r CCC: $37.00
Published on Web 10/11/2007

project on *T. thermophilus* HB8 (*10*). A homology search with FASTA (*11*) and CLUSTAL W (*12*) indicated that tHisPPase and HisPPases, which exhibit high sequence identities (more than 24%) with tHisPPase, have the four conserved motifs (His-h-His, h-x-x-His, Asp-Phe (or Tyr)-h-Ile-x-Ser-h-His, and h-h-h-x-x-Asp-x-His, where h is a hydrophobic residue and x is any residue) described above and another two conserved motifs: Gly-h-Glu and h-Gly-His-h-Asp. The histidine, aspartate, and glutamate residues in these motifs might be involved in the formation of the metal binding sites.

We expressed the gene in *E. coli*, purified the product protein, and confirmed that the recombinant enzyme has HisPPase activity (*13*). tHisPPase has 267 residues per subunit and a molecular weight of 29,976. In order to elucidate the overall fold, the active-site structure containing the metal center, substrate binding, and the reaction mechanism, we have determined the crystal structure of tHisPPase. Moreover, comparison of the metal center of tHisPPase with those of amidohydrolases and other phosphatases such as purple acid phosphatases and pyrophosphatases provides some insight into the catalytic mechanism for hydrolysis of the phosphate ester bond. The structure revealed that the C-terminal side of the $(\beta\alpha)_7$ barrel bears a trinuclear metal cluster consisting of a hydroxo-bridged dinuclear iron site and a zinc site that are liganded by six histidines, two aspartates, and one glutamate. In this paper, we report the first X-ray structural study on a monofunctional HisPPase belonging to the PHP family.

MATERIALS AND METHODS

Crystallization and Data Collection. Expression of tHisPPase by *E. coli*, purification of the expressed enzyme, enzyme assay, and crystallization of tHisPPase together with the preliminary crystallographic analysis were reported elsewhere (*13*). Briefly, crystals of tHisPPase·SO_4^{2-} were obtained at 293 K by equilibration of a mixture containing 2 μL of a 13 mg mL^{-1} protein solution and 2 μL of a reservoir solution comprising 1.5 M ammonium sulfate, 2% PEG400 (v/v), 1% MPD (v/v), and 100 mM Tris-HCl (pH 8.5) against 400 μL of reservoir solution. tHisPPase·PO_4^{2-} was crystallized at 293 K by mixing 2 μL of the 13 mg mL^{-1} protein solution with 2 μL of a reservoir solution comprising 0.68 M sodium malonate and 160 mM K_2HPO_4 (pH 8.0). The unliganded tHisPPase was crystallized at 293 K by mixing 2 μL of the 13 mg mL^{-1} protein solution with 2 μL of a reservoir solution comprising 0.68 M sodium malonate and 100 mM Tris-HCl (pH 8.5). Crystals of the sulfate and phosphate complexes and unliganded tHisPPase are isomorphous, with space group $P2_12_12$ and average cell dimensions of $a = 84.67$, $b = 97.06$, and $c = 74.52$ Å, with two subunits per asymmetric unit.

The X-ray diffraction data set for tHisPPase·SO_4^{2-} crystal was collected to 1.6 Å resolution at 100 K on the BL5A station at the Photon Factory (Tsukuba, Japan). The data sets for the tHisPPase·PO_4^{2-} crystal and the unliganded crystal were collected to 2.1 and 1.80 Å resolution, respectively, at 100 K on a Rigaku Raxis IV++ image-plate detector at a wavelength of 1.54 Å. The data were processed and scaled by use of the program HKL2000 (*14*). The heavy atom derivatives were obtained by soaking the tHisPPase·SO_4^{2-} crystal in solutions containing ~1 mM heavy atom reagents. The data sets for heavy atom derivatives were collected at 293 K on an Raxis IV++ image-plate detector, and were processed and scaled by use of the program Crystal Clear (Molecular Structure Corp., a Rigaku company).

Structure Determination and Refinement. The crystal structure of tHisPPase·SO_4^{2-} was solved at 1.6 Å resolution by the multiple isomorphous replacement method with four isomorphous data sets. The CCP4 program suite (*15*) was used for the scaling of all data and map calculations. The locations of the initial heavy atom sites were determined with SOLVE (*16*, *17*). The resulting MIR map has a mean figure of merit of 0.43. The map was improved by solvent flattering with RESOLVE to give a mean figure of merit of 0.68 (*17*). The initial polyalanine model was built into the electron density map by use of O (*18*) and refined with CNS (*19*). After density modification, nearly the entire backbone and most of the side chains could be traced by ARP/wARP (*20*) by use of 1.6 Å resolution data. The structure was then manually completed with program O. When the R_{factor} value decreased below 30%, a simulated annealing $2F_o - F_c$ map was calculated to assign metal ions and bound sulfates to the residual electron density. Solvent molecules were picked up from the σ_A-weighted $F_o - F_c$ map. Further model building and refinement cycles resulted in an R_{factor} of 0.202 and R_{free} of 0.221 (Table 1). The same refinement procedure was applied to tHisPPase·PO_4^{2-} and the unliganded tHisPPase but with the coordinates of tHisPPase·SO_4^{2-} as an initial model. Refinement cycles resulted in R_{factor} of 0.195 and 0.224 and R_{free} of 0.232 and 0.268 for tHisPPase·PO_4^{2-} and unliganded tHisPPase, respectively. Structure diagrams were drawn with MOLSCRIPT (*21*), POVSCRIPT+ (*22*), and PyMol (*23*).

Identification of Iron and Zinc Sites. The simulated annealing $2F_o - F_c$ map of tHisPPase·SO_4^{2-} showed a cluster of three marked electron density peaks per subunit in addition to sulfate ions. These three peaks were identified as those of two Fe ions and one Zn ion (Figure 1). An X-ray absorption experiment showed that the absorption edges of Fe and Zn were 1.7409 and 1.2832 Å, respectively. Multiwavelength anomalous diffraction data were collected at 100 K on the BL5A station at the Photon Factory (Tsukuba, Japan). Cell constants of the crystal were $a = 84.85$, $b = 97.25$, and $c = 74.69$ Å. Bijvoet data were obtained for four wavelengths at 1.2822 (Zn peak), 1.2899 (Zn low remote), 1.7395 (Fe peak), and 1.7533 Å (Fe low remote) before and after the absorption edges of Zn and Fe. The data were processed and scaled by use of the program HKL2000 (*14*). Anomalous data collection statistics are available as Supporting Information.

Dynamic Light Scattering. Molecular weight measurements were performed at 293 K via dynamic light scattering (DynaPro-801, Protein Solutions) by injecting a 15 μL of protein solution (20 mM HEPES-NaOH, pH 7.5). The protein sample exhibited a monomodal distribution and the molecular weight was estimated to be 118 000.

Enzyme Assay. Enzymatic activity was measured by monitoring the inorganic phosphate released from histidinol phosphate by a previously reported procedure (*24*). The reaction buffers contained a series of concentrations of histidinol phosphate (0.1, 0.2, 0.4, 0.6, 0.8, and 1.0 mM) in 50 mM Tris-HCl buffer (pH 8.8) at 310 K. The reaction was

Table 1: Data Collection and Refinement Statistics

	tHisPPase·SO_4^{2-}	tHisPPase·PO_4^{2-}	unliganded	Au1[a]	Pt1	Hg1	Hg2
			Diffraction Data				
wavelength (Å)	1.0	1.5418	1.5418	1.5418	1.5418	1.5418	1.5418
resolution (Å)	50.0−1.6	50.0−2.1	50.0−1.8	50−2.7	50−2.7	50−2.8	50−2.7
total no. of reflections	426 082	157 630	168 034	65 294	60 811	54 308	64 325
unique no. of reflections	81 599	48 379	57 365	34 054	34 015	30 393	34 139
redundancy	5.2 (4.6)[b]	3.3 (3.2)	2.9 (2.4)	1.9 (1.9)	1.8 (1.7)	1.8 (1.7)	1.9 (1.8)
completeness (%)	99.0 (93.0)	99.6 (100.0)	99.2 (95.0)	99.3 (98.6)	99.3 (99.5)	98.1 (99.1)	99.2 (99.6)
$I/\sigma(I)$	42.9 (3.8)	24.2 (3.5)	7.6 (2.5)	8.5 (2.0)	7.8 (2.2)	8.0 (2.0)	10.1 (2.2)
R_{merge}[c] (%)	4.4 (30.3)	5.8 (27.4)	8.0 (33.7)	6.2 (28.7)	5.8 (27.3)	5.9 (26.0)	5.5 (26.1)
			MIR				
R_{diff}[d] (%)				13.2	11.2	14.6	13.4
no. of sites				3	2	1	1
phasing power[e]				1.13	0.46	0.63	0.54
			Refinement				
resolution limits (Å)	38.8−1.6	42.0−2.1	20.0−1.8				
R_{factor} (%)	20.2	19.5	22.4				
R_{free} (%)	22.1	23.2	26.8				
no. of solvent atoms	282	306	413				
deviations							
bond length (Å)	0.005	0.006	0.019				
bond angles (deg)	1.4	1.4	1.9				
mean *B* factor							
main-chain atoms (Å^2)	21.7	25.9	23.0				
side-chain atoms (Å^2)	23.6	27.2	24.1				
water atoms (Å^2)	31.4	34.8	32.0				
Ramachandran plot[f] (%)	93.8; 5.7; 0.5; 0.0	92.7; 6.4; 0.9; 0.0	92.2; 7.3; 0.5; 0.0				

[a] Heavy atoms derivatives: Au1, $KAu(CN)_2$; Pt1, K_2PtCl_4; Hg1, *p*-chloromercuribenzoic acid d; Hg2, Baker's dimercurial. [b] Values in parentheses are for the highest resolution shells: 1.66−1.60 Å in tHisPPase·SO_4^{2-}, 2.17−2.10 Å in tHisPPase·PO_4^{2-}, 1.86−1.80 Å in unliganded tHisPPase, 2.80−2.70 Å in Au1, Pt1, and Hg2, and 2.90−2.80 Å in Hg1. [c] $R_{merge} = \sum_{hkl} \sum_i |I_{hkl,i} - \langle I_{hkl} \rangle| / \sum_{hkl} \sum_i I_{hkl,i}$, where I = observed intensity and $\langle I \rangle$ = average intensity for multiple measurements. [d] $R_{diff} = \sum ||F_{PH}| - |F_P|| / \sum |F_P|$, where $|F_{PH}|$ and $|F_P|$ are the derivative and native structure-factor amplitudes, respectively. [e] Phasing power is the ratio of the rms of the heavy atom scattering amplitude and the lack of closure error. [f] Percentage of residues in the most favored, additionally allowed, generously allowed, and disallowed regions of a Ramachandran plot (*49*).

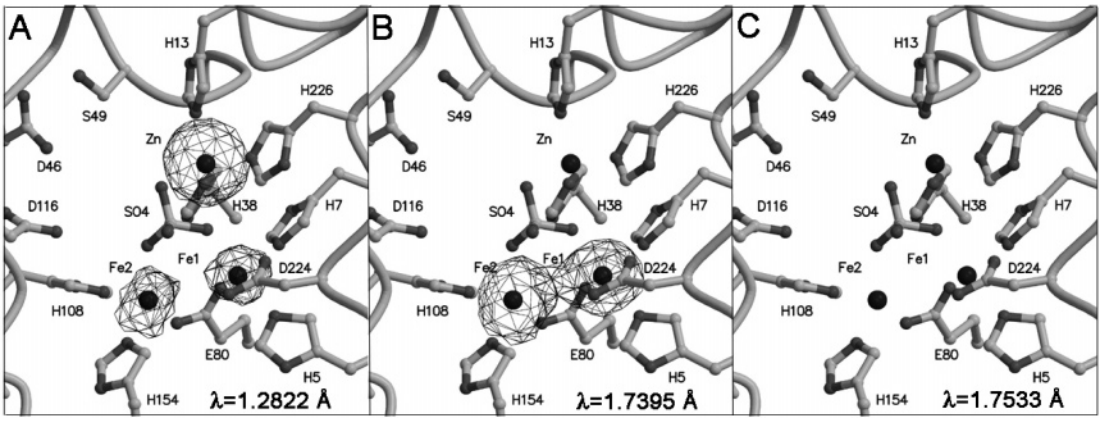

FIGURE 1: Bijvoet difference Fourier maps at 1.8 Å resolution. The anomalous electron density maps contoured at 5.0σ were calculated from Bijvoet data at (A) λ = 1.2822 Å, (B) λ = 1.7395 Å, and (C) λ = 1.7533 Å.

initiated by adding 5 μL of tHisPPase solution (20 mM Tris-HCl, 0.04 mg mL^{-1} tHisPPase) to 80 μL of reaction buffer and terminated by the addition of 20 μL of malachite green reagent solution. k_{cat}, K_m, and k_{cat}/k_m values for tHisPPase were calculated to be 0.93 ± 0.004 s^{-1}, 0.27 ± 0.02 mM, and 3.44 ± 0.17 s^{-1} mM^{-1}, respectively. The protein concentration was estimated by the method of Bradford (*25*).

RESULTS AND DISCUSSION

Overall Structure. The overall structure of tHisPPasePO_4^{2-} is shown in Figure 2A. The molecular mass of the enzyme was estimated to be 118 kDa by dynamic light scattering analysis (DynaPro, Protein Solutions). tHisPPase forms a tetramer with a crystallographic 2-fold axis in the crystal. The enzyme thus exists as a homotetramer with 222 symmetry. One subunit in the tetramer interacts with the other two subunits, and the surface areas of the subunit interfaces are 971 Å^2 for subunits I and II and 880 Å^2 for subunits I and I′ (Figure 2A). All the subunit interfaces are distant from the active sites and not essential for the catalytic activity.

The subunit structure of tHisPPase is shown in Figure 2B,C together with the secondary structure assignments made with program DSSP (*26*). When the Cα carbon atoms are superimposed between subunits in the asymmetric units, the rms deviations are 0.12, 0.13, and 0.13 Å for tHisPPase·SO_4^{2-}, tHisPPase·PO_4^{2-}, and unliganded tHisPPase, respectively. This indicates that the overall structures of the two subunits

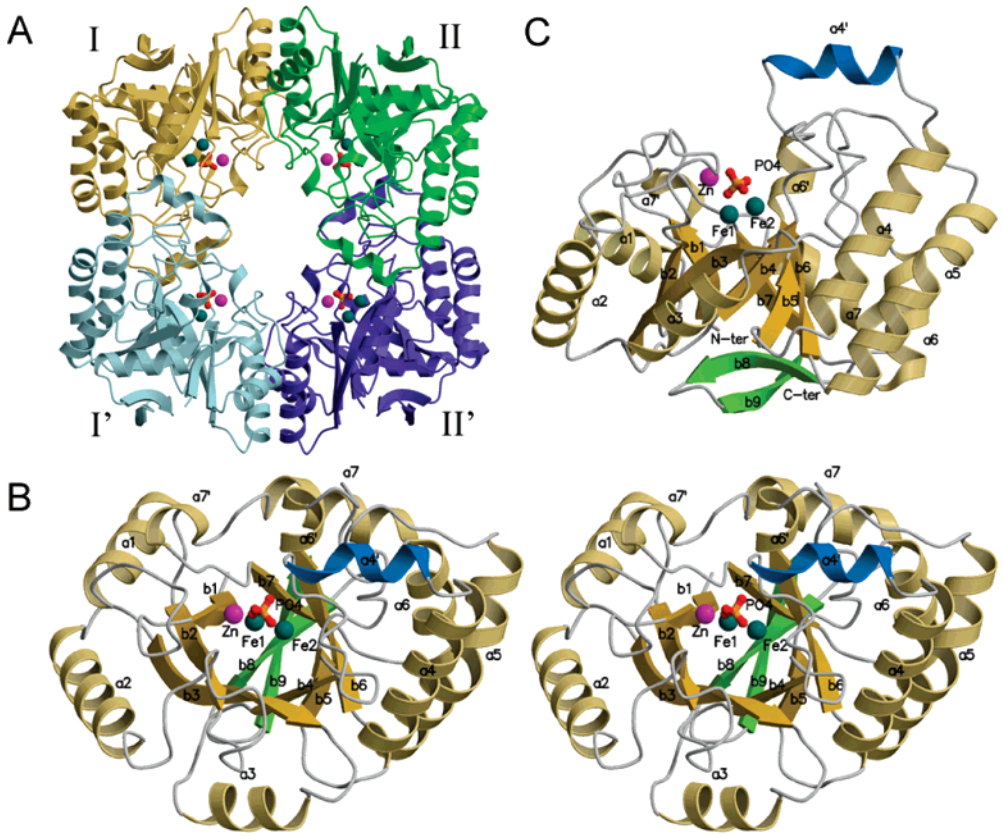

FIGURE 2: Ribbon structural drawing of tHisPPase complexed with a phosphate ion. Fe and Zn ions are presented as green and magenta circles, and the phosphate ion is shown as a ball-and-stick model. (A) View of the tHisPPase tetramer viewed down the molecular 2-fold axis. Subunits I, II, I′, and II′ are represented by brown, green, pale blue, and deep blue ribbons, respectively. Subunits I and II reflect the coordinates in the asymmetric unit. Subunits I′ and II′ are the crystallographic equivalents of subunits I and II, respectively. The active-site crevice faces the hole formed at the center of the molecule. (B) Stereoview of the subunit with secondary structure assignments showing the distorted $(\beta\alpha)_7$ barrel. The β-strands of the barrel, the α-helices of the barrel, the linker, and the C-terminal tail are shown as yellow, orange, blue, and green ribbons, respectively. β-Strands are denoted by b1−b9 and α-helices by a1−a7. The N and C termini are labeled. (C) Side view of the subunit with secondary structure assignments. The image structure is turned 90° clockwise around the horizontal axis relative to the image in panel B.

in an asymmetric unit are quite similar. The subunit Cα carbon atoms are fitted between tHisPPase·SO_4^{2-}, tHisPPase·PO_4^{2-}, and unliganded tHisPPase to give an average rms deviation of 0.31 Å with a maximum rms deviation of 0.36 Å, indicating that the overall subunit structures are essentially the same between three enzyme forms.

The subunit is divided into a barrel, a linker (Tyr109−Arg127), and a C-terminal tail (Arg248−Pro262). The barrel has a distorted $(\beta\alpha)_7$ structure (β-strand b1, α-helix a1, β-strand b2, α-helix a2, ..., β-strand b7, and α-helix a7). The linker (α-helix a4′ and its N-terminal loop) is inserted between β-strand b4 and α-helix a4 hanging over the C-terminal side of the barrel. The C-terminal tail consists of a two-stranded antiparallel β-sheet. The large crevice for binding of the substrate histidinol phosphate is formed on the C-terminal side of the barrel and is surrounded by the loops between β-strand b1 and α-helix a1, β-strand b2 and α-helix a2, and β-strand b4 and α-helix a4.

Active-Site Structure and Metal Coordination. The active-site components and bound metal ions in tHisPPase·PO_4^{2-} and unliganded tHisPPase are shown in Figure 3 panels A and B. A schematic drawing of the metal ligation is displayed in Figure 4. The simulated annealing $2F_o - F_c$ map of tHisPPase·SO_4^{2-} showed a cluster of three marked electron density peaks per subunit in addition to sulfate ions. These three peaks were identified as those of two Fe ions and one Zn ion in anomalous scattering experiments, although Fe and Zn ions were not present in the buffer solution used for purification or crystallization. The absorption edges of Fe and Zn were determined to be 1.7409 and 1.2832 Å, respectively, in an X-ray absorption experiment. Three electron density peaks were observed on a Bijvoet difference map based on the data at $\lambda = 1.2822$ Å, whereas there were only two peaks based on the data at $\lambda = 1.2899$ or 1.7395 Å, indicating that the missing peak corresponds to the Zn ion (Figure 1). No significant peak was observed on the map calculated at $\lambda = 1.7533$ Å. The remaining two peaks were thus assigned to Fe ions. Anomalous scattering experiments were also performed on the unliganded tHisPPase crystal, which confirmed that the two Fe ions and one Zn ion are located at the same places as those in tHisPPase·SO_4^{2-}. The metal-ion compositions of tHisPPase were determined by Rigaku Corp. SPECTRO CIROS CCD CIROS-160EOP inductively coupled plasma (ICP) spectrometry. Analysis of the protein solution (54.5 μg mL^{-1}) revealed a Fe ion/tHisPPase ratio of 1.94:1.00, a Zn ion/tHisPPase ratio of 0.94:1.00, and a Fe ion/Zn ion ratio of 2.07:1.00. The levels of contaminating ions were below the detectable limits.

The active site of tHisPPase·PO_4^{2-} is characterized by a trinuclear metal cluster with Fe1−Fe2, Fe1−Zn, and Fe2−Zn distances of 3.47, 4.70, and 5.84 Å, respectively (Figures 3A and 4). The Fe1, Fe2, and Zn ions, which are in close

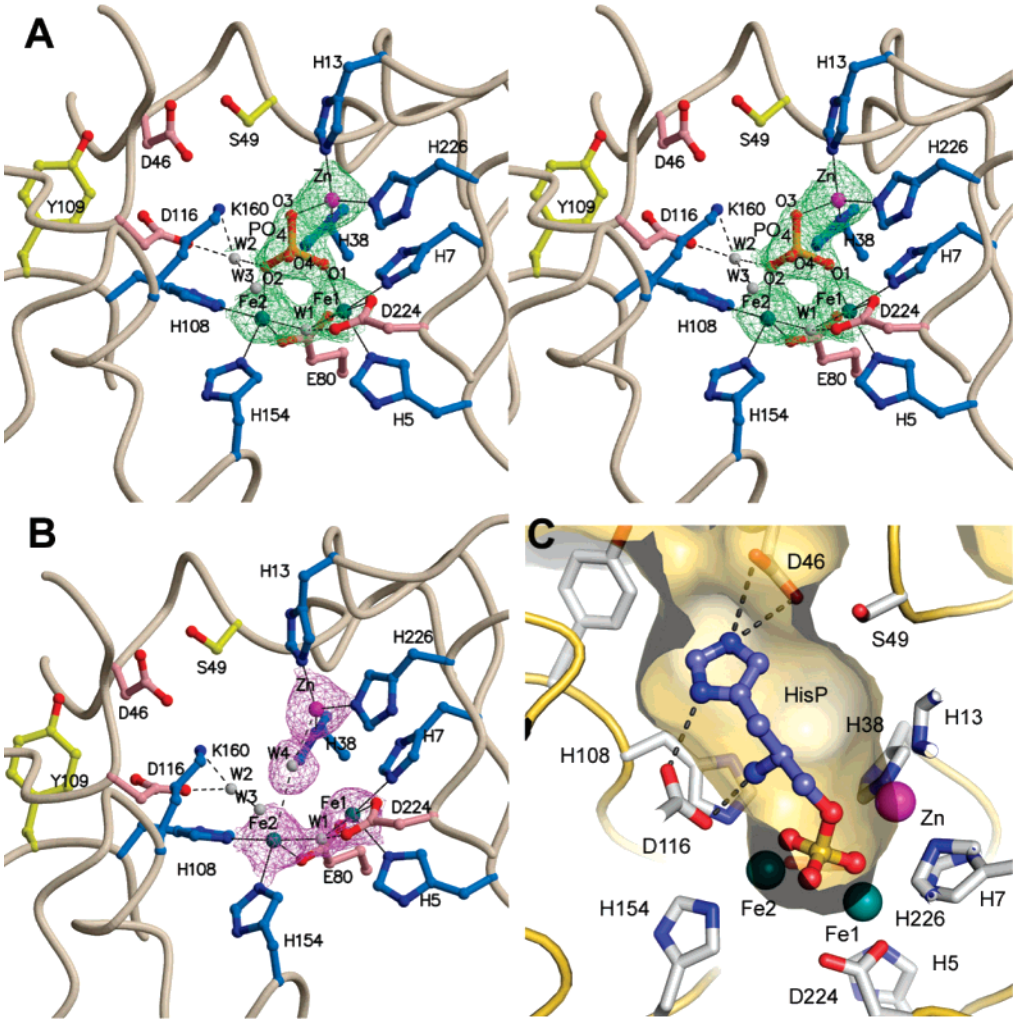

FIGURE 3: Active-site structures. (A) Stereoview of the active-site structure in tHisPPase·PO_4^{2-}. Fe ions, Zn ion, and water molecules (W1−−W3) are presented as green, magenta, and gray circles. The phosphate ion and active-site residues are shown as ball-and-stick models. Thin and dotted lines represent coordination and hydrogen bonds, respectively. The $2F_o - F_c$ electron density map contoured at 1.0 σ is calculated from the final model with the trinuclear metal center and the phosphate ion omitted. (B) View of the active-site structure in the unliganded tHisPPase. The structure is quite similar to that of tHisPPase·PO_4^{2-}. The $2F_o - F_c$ electron density map is contoured at 1.0σ. (C) Complex model between tHisPPase and the substrate histidinol phosphate. The substrate captured in the active site cavity is shown as a ball-and-stick model. The interactions of the substrate phosphate moiety with the metal center are the same as those shown in Figure 3A. Asp116 is hydrogen-bonded to the α-amino group and the N1 atom of the substrate imidazole group. Asp46 interacts with the N3 atom of the imidazole group.

proximity to each other, are located at metal sites M_1, M_2, and M_3, respectively, which are within 2.0−2.5 Å of histidine, aspartate, or glutamate residues. The Fe1 and Fe2 ions are bridged by a hydroxide ion, W1, which yields a hydroxo-bridged dinuclear metal center, and by the carboxylate of Glu80 in a bidentate manner, as observed in *B. subtilis N*-acetylglucosamine-6-phosphate deacetylase (NAGPase) (*27*). The phosphate ion originating from the crystallization buffer is liganded to all three metal ions. The Fe1 ion at metal site M_1 is liganded by N-3 nitrogens of His5 (2.2 Å) and His7 (2.3 Å), carboxylate oxygens of Glu80 (2.4 Å) and Asp224 (2.5 Å), bridging hydroxide W1 (2.1 Å), and O1 atom of the phosphate ion (2.3 Å) with octahedral geometry. The Fe2 ion at metal site M_2 is liganded by N-3 nitrogens of His108 (2.3 Å) and His154 (2.4 Å), carboxylate oxygen of Glu80 (2.3 Å), bridging hydroxide ion (2.0 Å), and O2 atom of the phosphate ion (2.2 Å) with distorted trigonal bipyramidal geometry. His108 and bridging hydroxide W1 act as axial ligands, and Glu80, His154, and phosphate ion form the vertices of three equatorial ligands. The Zn ion at metal site M_3 is liganded by N-3 nitrogens of His13 (2.3 Å), His38 (2.3 Å), and His226 (2.3 Å) and by the O3 atom of phosphate ion (2.1 Å) with distorted tetrahedral geometry. The bridging hydroxide ion is hydrogen-bonded to the carboxylate of Asp224, which is the ligand for metal site M_1. The O4 atom of the phosphate ion is hydrogen-bonded to W2, which interacts with Lys60, Asp116, and W3.

The four conserved motifs, which reside in the C-terminal half of β-strands or their C-terminal loops and characterize the PHP superfamily, are His5-h-His7 (C-terminal half of β-strand 1), h-x-Asp37-His38 (C-terminal half of β-strand 2), Asp101-Tyr102-h-Ile104-Gly104-Ser106-h-His108 (β-strand 4), and h-h-h-x-Ser223-Asp224-x-His226 (β-strand 7 and its C-terminal loop), where h is hydrophobic residue and x is any residue. Histidine residues and Asp224 of the motifs act as ligands for metal sites M_1 (His5, His7, and Asp224), M_2 (His108), and M_3 (His38 and His226). The remaining residues on β-strands form the base for the metal sites. In addition to these motifs, another two motifs, h-Glu80-x-Asp82 (C-terminal half of β-strand 3) and His154-h-Asp156-

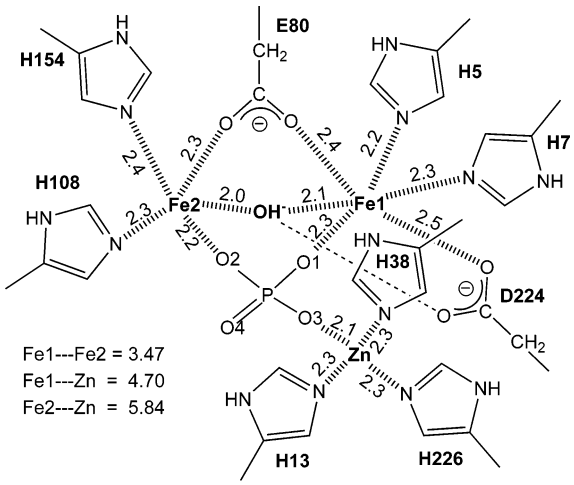

FIGURE 4: Schematic drawing of metal−ligand interactions in the active site. Hatched lines are coordination bonds and the corresponding bond lengths are shown in angstroms. Metal−metal distances are also indicated. A dotted line represents the hydrogen bond between Asp224 and the bridging hydroxide.

h−h-Lsy159 (loop between β-strand 5 and α-helix 5), are well conserved in monofunctional HisPPases. Glu80 is the bidentate ligand that bridges metal sites M_1 and M_2, and His154 is the ligand for metal site M_2. These six motifs conserved in monofunctional HisPPases are combined to produce metal binding sites M_1, M_2, and M_3 for tHisPPase catalysis.

The active-site structure of the unliganded tHisPPase is quite similar to that of tHisPPase·PO_4^{2-} except that the phosphate ion is replaced by a water molecule, W4 (Figure 3B). Water molecule W4 is at distances of 3.4, 3.1, and 3.1 Å from the Fe1, Fe2, and Zn ions, respectively. The trinuclear metal cluster is liganded by the bridging hydroxide ion (W1) and active-site residues in the same manner as that in tHisPPase·PO_4^{2-}. No significant differences in active-site structures were observed between tHisPPase·PO_4^{2-} and tHisPPase·SO_4^{2-}.

Structural Comparison of PHP Proteins and Amidohydrolases. Program DALI (*28*) was used to search the Protein Data Bank for proteins possessing three-dimensional structures similar to that of tHisPPase. The highest *Z* scores (strength of structure similarity) were calculated to be 20.4 for hypothetical YcdX protein from *E. coli* (*5*), 14.1 for *P. horikoshii* ribonuclease P protein Ph1877p (*7*), 12.5 for *Agrobacterium tumefaciens* imidazolone propionase (PDB code 2GOK), 12.0 for *E. coli* cytosine deaminase (*29*), 10.2 for *E. coli* NAGPase (*30*), 10.2 for *E. coli* isoaspartyl dipeptidase (*31*), 10.0 for *E. coli* TatD homologue (PDB code 1ZZM), and 9.9 for the PHP domain of DNA polymerase III from *T. aquaticus* (*6*). The DALI results and conserved metal site residues are listed in order of *Z* values in Table 2 together with those for *Pseudomonas diminuta* phosphotriesterase (*32*), *B. subtilis* NAGPase (*27*), *E. coli* dihydroorotase (*33*), and *Alcaligenes faecalis* D-aminocylase (*34*), which have metal sites M_1 and M_2 similar to those of tHisPPase. The proteins listed in Table 2 belong to the PHP family or the amidohydrolase superfamily. tHisPPase, hypothetical YcdX protein, ribonuclease P protein component 3, and the PHP domain of DNA polymerase III are members of the PHP family; the remaining proteins are members of the amidohydrolase superfamily. Hypothetical YcdX protein is a putative phosphoesterase (*5*). Protein Ph1877p is essential for ribonuclease P activity (*35*). TatD and the PHP domain of DNA polymerase III exhibit metal-dependent nuclease activity (*6*, *36*) catalyzing the hydrolysis of a phosphoester bond. The amidohydrolases catalyze the hydrolysis of carbon−nitrogen bonds in amido or amino groups and phosphoester bonds (*29*, *31*, *37*, *38*).

Holm and Sander (*8*) first demonstrated the existence of the amidohydrolase superfamily, which have a distorted $(\beta\alpha)_8$ barrel fold bearing metal sites consisting of conserved histidine and aspartate residues. Aravind and Koonin (*4*) pointed out that the conserved residues in the PHP family exhibit similarity to those in the amidohydrolase superfamily. The PHP proteins listed in Table 2 have a distorted $(\beta\alpha)_7$ barrel structure although one of the barrel β-strands in DNA polymerase III runs antiparallel, while amidohydrolases fold into a distorted $(\beta\alpha)_8$ TIM-barrel fold (*9*). The Cα atoms superimposition of the PHP protein onto the amidohydrolases shows that β-strands 1−2 and 4−7 of the $(\beta\alpha)_7$ barrel fit β-strands 1−2 and 5−8 of the $(\beta\alpha)_8$ barrel, respectively (Figure 5A). The long β-strand 3 of the $(\beta\alpha)_7$ barrel extends from β-strand 3 to β strand 4 of the $(\beta\alpha)_8$ barrel with the N- and C-terminal sides of β-strand 3 overlapping with β-strands 3 and 4 of the $(\beta\alpha)_8$ barrel, respectively. This suggests that the $(\beta\alpha)_8$ barrel of amidohydrolases has evolved from the $(\beta\alpha)_7$ barrel of the PHP family proteins or vice versa, although convergent evolution cannot be completely excluded because residues other than the metal site ones are not conserved in the two families. Although the amino acid residues of an ancestor protein are extensively divergent, the barrel fold, especially the fold of the barrel inside, is maintained to produce the base of the metal center, which is essential for catalysis of the hydrolysis reaction.

Interestingly, the metal center located at the C-terminal side of the $(\beta\alpha)_8$ barrel in amidohydrolases is a counterpart of metal site M_1 or metal sites M_1 and M_2 (dinuclear metal center) in tHisPPase, hypothetical protein YcdX, and the PHP domain of DNA polymerase III (Figure 5A). Cytosine deaminase has metal site M_1 in which the Fe1 ion is surrounded by the residues conserved in PHP family proteins (*29*) (Table 2). The metal center of *B. subtilis* NAGPase is a copy of the hydroxo-bridged dinuclear iron center observed in tHisPPase (*27*) (Figure 5A). The amino acid residues coordinated to Fe ions and the coordination geometries around Fe ions are conserved between NAGPase and tHisPPase. These results imply that the trinuclear metal center associated with hydrolysis of the phosphoester bond in the PHP family is closely related to the mononuclear or dinuclear metal center in amidohydrolases. Metal site M_1 is the most common in all proteins cited in Table 2, followed by metal site M_2. Metal site M_3 is not conserved and seems to be necessary for the hydrolysis of the phosphoester bond.

Hypothetical protein YcdX belonging to the PHP family exhibits the highest *Z* value and sequence identity with tHisPPase, as shown in Table 2 (*5*). The main-chain Cα atoms of YcdX are superimposed on those of tHisPPase, indicating that the barrel β-strands of the two proteins have very similar arrangements (Figure 5B), while the α-helices and some of the loops connecting β-strands are different in length and/or in location, and the linker hanging over the active-site crevice is missing in YcdX. The ligand residues for the trinuclear metal cluster in tHisPPase are completely

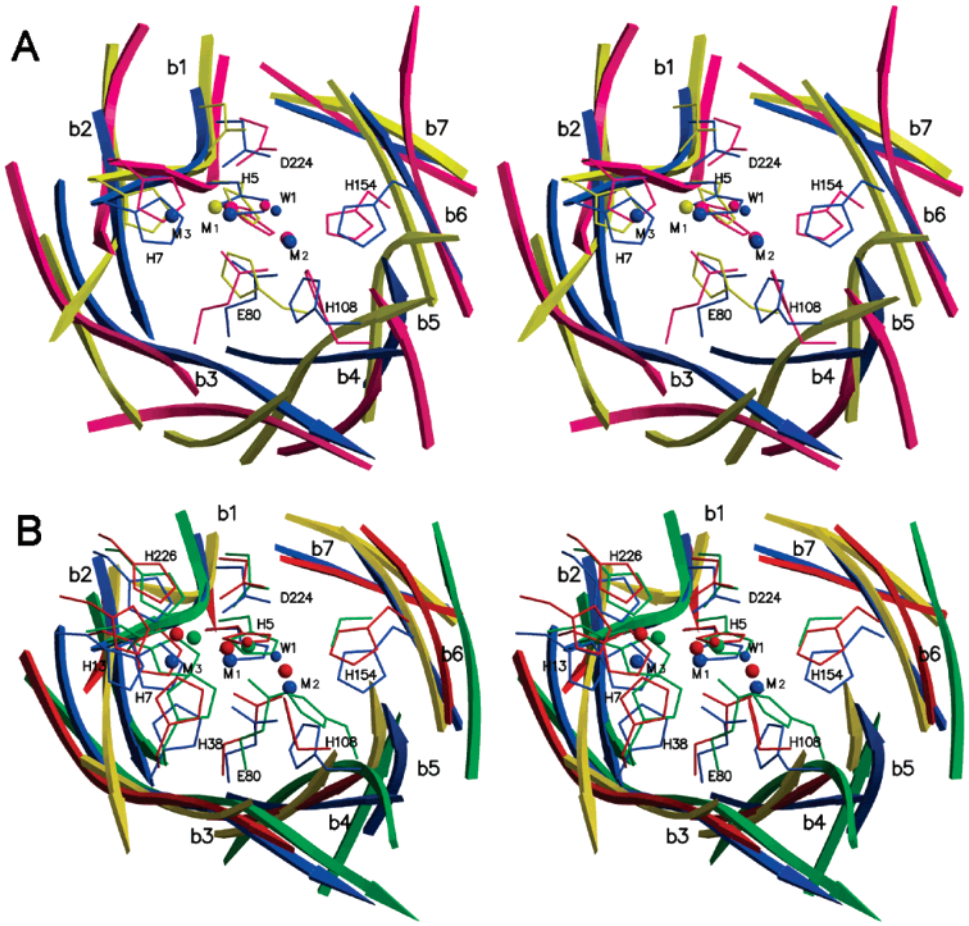

FIGURE 5: Comparison of barrel structures, metal sites, and ligand residues in PHP proteins and amidohydrolases. Barrel β-strands, metal ions, bridging hydroxides, and ligand residues to the metal center are shown by arrows, large circles, small circles, and lines, respectively. β-strands 1−7 in tHisPPase are labeled as b1−b7. (A) Superpositioning of Cα atoms of tHisPPase onto amidohydrolases. tHisPPase, cytosine deaminase, and NAG are presented in deep blue, yellow, and red, respectively. β-Strand b3 of tHisPPase ranges from β-strand b3 to b4 in amidohydrolases. The hydroxo-bridged dinuclear iron center in tHisPPase is conserved in NAG. (B) Superpositioning of Cα atoms of tHisPPase onto PHP proteins. tHisPPase, hypothetical YcdX protein, ribonuclease P protein Ph1877p, and the PHP domain of DNA polymerase III are presented in deep blue, red, yellow, and green, respectively. Metal sites M_1, M_2, and M_3 are conserved except in ribonuclease P protein.

Table 2: DALI Results and the Conserved Metal Site Residues Compared with Those of tHisPPase

					M_1[b]			$M_{1,2}$	M_2		M_3		
protein name	PDB code	*Z*-value	sequence identity (%)	RMSD[a] (Å)	H5	H7	D224	E80[c]	H108	H154	H13	H38	H226
hypothetical YcdX protein	1m65	20.2	23	2.7	+[d]	+	+	+	+	+	+	+	+
RNase P protein Ph1877p	1v77	14.1	9	2.9	−[e]	−	−	−	−	−	−	−	−
imidazolone propionase	2gok	12.5	14	3.1	+	+	+	H[f]	−	+	Y	+	N
cytosine deaminase	1k6w	12.0	12	3.4	+	+	+	H[f]	−	−	−	−	−
NAGPase from *E. coli*[g]	1ymy	10.2	16	3.7	Q	N	+	+	+	+	−	−	−
isoaspartyl dipeptidase	1po9	10.2	16	3.5	+	+	+	+[h]	+	+	−	−	−
TatD homologue	Lzzm	10.0	15	3.4	+	+	+	+	+	+	−	−	−
PHP domain of Pol III[i]	2hpm	9.9	20	3.5	+	+	+		+	C	D	+	+
phosphotriesterase	Ldpm	9.4	17	3.7	+	+	+	+[h]	+	+	−	−	−
NAGPase from *B. subtilis*	Lun7	8.9	15	3.8	+	+	+	+	+	+	−	−	−
dihydroorotase	Lj79	8.6	11	4.1	+	+	+		+	+	−	−	−
D-aminocyclase	Irk6	7.6	17	3.6	+	+	+	C[j]	+	+	−	−	−

[a] Root-mean-square deviation. [b] Residues H5, H7, D224, and E80 form the metal site 1 (M_1) in tHisPPase. [c] E80 is involved in both metal sites M_1 and M_2. [d] (+) indicates that the corresponding residue is conserved. [e] (−) indicates that the corresponding ligand residue is not observed. [f] E80 is replaced by histidine, which is the ligand residue for M_1. [g] The enzyme binds a single metal at the M_2 position (*30*). [h] E80 is replaced by a carboxylated lysine, which is the ligand for metal sites M_1 and M_2. [i] DNA polymerase III. [j] E80 is replaced by cysteine, which is the ligand residue for M_2.

conserved in YcdX. Zn ions originating from the crystallization buffer are bound to three metal sites in YcdX. The phosphate ions derived from the crystallization buffer reside on the solvent side of the active site but are not liganded to Zn ions. The hydroxide ion bridging metal sites M_1 and M_2 is located at a position different from that in tHisPPase, resulting in the trigonal bipyramidal and tetrahedral geometries of the coordination in metal sites M_1 and M_2, respectively. The different behavior of phosphate and hydroxide ions between YcdX and tHisPPase may be

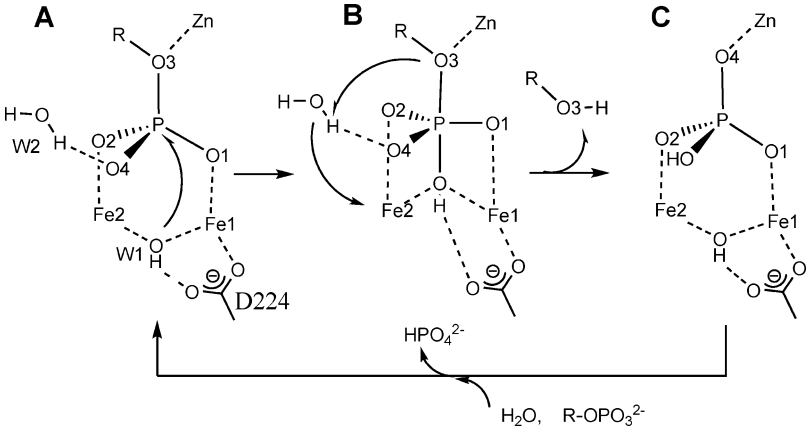

FIGURE 6: Proposed reaction mechanism. W1 and W2 correspond to those shown in Figure 3A. The bridging hydroxide (W1) makes a direct attack on the phosphorus atom of the substrate phosphate.

attributed to the difference in metals bound to sites M_1 and M_2. When the metal sites of YcdX are liganded by inherent metals, the phosphate ion might be liganded to three metals to reproduce the metal cluster observed in tHisPPase. In that case, YcdX might hydrolyze a phosphoester bond like tHisPPase but might have a different substrate specificity because the residues surrounding the active center are not conserved.

Ribonuclease P protein Ph1877p, which is classified into the PHP family, is unusual in that it does not retain any of the four motifs that characterize the PHP family but has an arrangement of β-strands in the $(\beta\alpha)_7$ barrel similar to that in tHisPPase in spite of the low sequence identity of 8% (*7*). The amino acid residues associated with the enzymatic activity of the ribonuclease P are distributed on the surface of the protein, which is consistent with the lack of the metal sites formed at the crevice on the C-terminal side of the barrel. The imidazolone propionase belonging to the amidohydrolase superfamily ($Z = 16.1$, sequence identity = 6%) was shown to have the most similar fold to that of protein Ph1877p but there is no significant identity in the sequences of the two proteins, which is reminiscent of the high structural similarity and low sequence identity between protein Ph1877p and tHisPPase.

The PHP domain of DNA polymerase III is representative of the PHP family together with HisPPase (*6*). The protein exhibits the second highest sequence identity of 20% with tHisPPase and retains the three metal sites liganded by conserved residues similar to those in tHisPPase and YcdX, although the *Z* value is relatively low. This implies that the nuclease activity which hydrolyzes the phosphodiester bond favors a trinuclear metal center like that in tHisPPase. β-strand 4 of the PHP domain is antiparallel to the other six β-strands of the $(\beta\alpha)_7$ barrel. Nevertheless, the β-strands of the barrel are arranged similarly to those in tHisPPase (Figure 5B).

Mechanistic Implication. The hydroxo-bridged dinuclear metal center (metal sites M_1 and M_2) of tHisPPase is commonly observed in metal-dependent amidohydrolases, in which metal sites M_1 and M_2 are bridged by a hydroxide ion and bidentately by a carboxylate group (*9*, *27*, *32*, *33*, *39*, *40*). The mechanism of the amidohydrolases, especially dihydroorotase and phosphotriesterase, has been investigated in detail (*32*, *33*). The main point of the mechanism proposed is that the bridging hydroxide ion is a direct nucleophile to the carbonyl carbon atom in the amide bond or the phosphorus atom in the P−O bond to be hydrolyzed, and the invariant aspartate (Asp224 in tHisPPase), which is liganded to M_1 and is hydrogen-bonded to the bridging hydroxide, acts as an acid−base catalyst (Table 2).

A hydroxo-bridged dinuclear metal center is also found in a number of phosphatases, especially in purple acid phosphatases and pyrophosphatases, and is assumed to result from convergent evolution to catalyze the common hydrolysis reaction (*41*). The basic events that occur in the hydrolysis of the phosphoester bond is the in-line attack by the nucleophile (hydroxide ion) on the phosphorus atom from the opposite side of the leaving group, formation of a trigonal bipyramidal pentacoordinate intermediate in which the nucleophile and the leaving group act as axial ligands, and release of the leaving group. In the case of purple acid phosphatases, two mechanisms have been proposed on the basis of spectroscopic and crystallographic works and are still under debate (*41*−*43*). One is the nucleophilic attack by a hydroxide ion terminally bound to the dinuclear metal center on the phosphate monodentately liganded to the other metal of the center (*42*). The other, which we favor, is the nucleophilic attack of the bridging hydroxide on the phosphate bidentately liganded to both metals of the dinuclear center (*41*, *43*). As for the mechanism in pyrophosphatases, the latter is the predominant mechanism although there are also two mechanisms proposed (*44*−*46*).

The coordination geometry of the phosphate−trinuclear metal center complex in tHisPPase·$PO4^{2-}$ is a suitable one for the hydrolysis reaction to proceed through the latter mechanism described above, although there is no direct evidence that the phosphate moiety of the substrate interacts with the metal center similarly to the phosphate ion. The bridging hydroxide (W1) is at a distance of 3.3 Å from the phosphorus atom of the phosphate ion and is in the opposite direction from the P−O3 bond with W1−P−O3 = 172° (Figure 3). The Zn ion at metal site M_3 interacts with the O3 atom and is a potential acid catalyst if the O3 atom is the phosphoester oxygen.

The substrate was modeled into the active site such that the phosphate moiety is bound to the trinuclear metal center in a manner similar to the phosphate ion in tHisPPase·PO_4^{2-} crystal structure (Figure 3C). The phosphate ion is replaced by the substrate phosphate, with the phosphate O3 atom corresponding to the phosphoester oxygen of the substrate.

Asp116, which interacts with the O4 atom of the phosphate ion in the medium of W2, is the most probable candidate that forms a hydrogen bond/salt bridge with the amino group of the substrate (Figure 3). The substrate imidazole group was placed so as to interact with Asp46 and Asp116. The model structure was optimized with CHARMm by use of the default minimize protocol of Discovery Studio 1.6 (Accelrys, San Diego, CA) (*47*). The constraints were applied to the distances between the trinuclear metal cluster and the coordinated atoms. The substrate model fits well the active-site crevice (Figure 3C) and has reasonable conformational angles.

The catalytic mechanism proposed for tHisPPase in Figure 6 is based on the X-ray structures of tHisPPase, the enzyme−substrate complex model described above, and mechanistic consideration of the reaction, previously reported for amidohydrolases and pyrophosphatases. The active-site structure of the unliganded enzyme is quite similar to that of tHisPPase·PO_4^{2-} except that the phosphate ion in the complexed enzyme is replaced by a water molecule (W4) (Figure 3A,B). Upon the approach of the substrate to the active site, the substrate phosphate takes the place of the water molecule, W4, to be liganded to the trinuclear metal site and to form the enzyme−substrate complex (Figure 6A). The bridging hydroxide is activated by two Fe ions and by hydrogen-bonding to the carboxylate of Asp224. The electrophilicity of the phosphorus atom is enhanced by the interactions with the three metal ions. The bridging hydroxide, the phosphorus atom, and the phosphate O3 atom are in line. The bridging hydroxide ion then makes a nucleophilic attack on the phosphorus atom to form the trigonal bipyramidal transition state, which would be stabilized through maintenance of the interactions of the phosphate with the metal center as much as possible (Figure 6B). The geometrical constraint of the transition state makes the phosphorus atom move slightly toward the W1 atom to loosen the P−O3 bond (*48*), which is polarized by the Zn ion as the acid catalyst. A plausible candidate for the proton donor for the substrate O3 is water molecule W2, which is close to the metal center. W2 is polarized by interactions with Lys160, Asp116, water molecule W3, and the substrate O4 atom and is at a distance of 3.6 Å from the substrate O3. W2 adds its proton to the substrate O3 to release histidinol and to generate a hydroxide ion (Figure 6B,C). The resultant hydroxide ion might reproduce the hydroxo-bridged dinuclear metal center as shown in Figure 3B. The substrate enters the active site to liberate the phosphate ion to form the enzyme−substrate complex (Figure 6A).

In summary, we have determined the crystal structures of monofunctional tHisPPase as tHisPPase·SO_4^{2-}, tHisPPase·PO_4^{2-}, and unliganded tHisPPase at 1.6, 2.1, and 1.8 Å resolution, respectively. The sulfate or phosphate ion derived from the crystallization buffer is liganded to a trinuclear metal center consisting of a hydroxo-bridged dinuclear iron cluster and a Zn ion. The $(\beta\alpha)_7$ barrel fold and the trinuclear metal center are correlated with the $(\beta\alpha)_8$ barrel and the metal center in amidohydrolases, respectively. The architecture of the phosphate−metal center complex supports a direct attack of the bridging hydroxide on the substrate phosphate in the hydrolysis of the phosphoester bond.

SUPPORTING INFORMATION AVAILABLE

Anomalous data collection statistics. This material is available free of charge via the Internet at http://pubs.acs.org.

REFERENCES

1. Voet, D., and Voet, J. (2004) *Biochemistry*, John Wiley & Sons Inc., New York.
2. le Coq, D., Fillinger, S., and Aymerich, S. (1999) Histidinol phosphate phosphatase, catalyzing the penultimate step of the *histidine biosynthesis pathway, is encoded by ytvP (hisJ) in Bacillus* subtilis, *J. Bacteriol. 181*, 3277−3280.
3. Thaller, M. C., Schippa, S., and Rossolini, G. M. (1998) Conserved sequence motifs among bacterial, eukaryotic, and archaeal phosphatases that define a new phosphohydrolase superfamily, *Protein Sci. 7*, 1647−1652.
4. Aravind, L., and Koonin, E. V. (1998) Phosphoesterase domains associated with DNA polymerases of diverse origins, *Nucleic Acids Res. 26*, 3746−3752.
5. Teplyakov, A., Obmolova, G., Khil, P. P., Howard, A. J., Camerini-Otero, R. D., and Gilliland, G. L. (2003) Crystal structure of the *Escherichia coli* YcdX protein reveals a trinuclear zinc active site, *Proteins: Struct., Funct., Genet. 51*, 315−318.
6. Bailey, S., Wing, R. A., and Steitz, T. A. (2006) The structure of *T. aquaticus* DNA polymerase III is distinct from eukaryotic replicative DNA polymerases, *Cell 126*, 893−904.
7. Takagi, H., Watanabe, M., Kakuta, Y., Kamachi, R., Numata, T., Tanaka, I., and Kimura, M. (2004) Crystal structure of the ribonuclease P protein Ph1877p from hyperthermophilic archaeon *Pyrococcus horikoshii* OT3, *Biochem. Biophys. Res. Commun. 319*, 787−794.
8. Holm, L., and Sander, C. (1997) An evolutionary treasure: unification of a broad set of amidohydrolases related to urease, *Proteins: Struct., Funct., Genet. 28*, 72−82.
9. Seibert, C. M., and Raushel, F. M. (2005) Structural and catalytic diversity within the amidohydrolase superfamily, *Biochemistry 44*, 6383−6391.
10. Yokoyama, S., Hirota, H., Kigawa, T., Yabuki, T., Shirouzu, M., Terada, T., Ito, Y., Matsuo, Y., Kuroda, Y., Nishimura, Y., Kyogoku, Y., Miki, K., Masui, R., and Kuramitsu, S. (2000) Structural genomics projects in Japan, *Nat. Struct. Biol. 7 (*Suppl.), 943−945.
11. Pearson, W. R., and Lipman, D. J. (1988) Improved tools for biological sequence comparison, *Proc. Natl. Acad. Sci. U.S.A. 85*, 2444−2448.
12. Thompson, J. D., Higgins, D. G., and Gibson, T. J. (1994) CLUSTAL W: improving the sensitivity of progressive multiple sequence alignment through sequence weighting, position-specific gap penalties and weight matrix choice, *Nucleic Acids Res. 22*, 4673−4680.
13. Omi, R., Goto, M., Nakagawa, N., Miyahara, I., and Hirotsu, K. (2004) Expression, purification and preliminary X-ray characterization of histidinol phosphate phosphatase, *Acta Crystallogr. D60*, 574−576.
14. Otowinowski, Z., and Minor, W. (1997) Processing of X-ray diffraction data collected in oscillation mode, *Methods Enzymol. 276*, 307−326.
15. CCP4. (1994) The CCP4 suite: programs for protein crystallography, *Acta Crystallogr. D50*, 760−763.
16. Terwilliger, T. C., and Berendzen, J. (1999) Automated MAD and MIR structure solution, *Acta Crystallogr. D55*, 849−861.
17. Terwilliger, T. C. (2003) Automated main-chain model building by template matching and iterative fragment extension, *Acta Crystallogr. D59*, 38−44.
18. Jones, T. A., Zou, J. Y., Cowan, S. W., and Kjeldgaard, M. (1991) Improved Methods for Building Protein Models in Electron-Density Maps and the Location of Errors in These Models, *Acta Crystallogr. A47*, 110−119.
19. Brunger, A. T., Adams, P. D., Clore, G. M., DeLano, W. L., Gros, P., Grosse-Kunstleve, R. W., Jiang, J. S., Kuszewski, J., Nilges, M., Pannu, N. S., Read, R. J., Rice, L. M., Simonson, T., and Warren, G. L. (1998) Crystallography & NMR system: A new software suite for macromolecular structure determination, *Acta Crystallogr. D54*, 905−921.
20. Morris, R. J., Perrakis, A., and Lamzin, V. S. (2002) ARP/wARP's model-building algorithms. I. The main chain, *Acta Crystallogr. D58*, 968−975.

21. Kraulis, P. J. (1991) MOLSCRIPT: a program to produce both detailed and schematic plots of protein structures, *J. Appl. Crystallogr. 24*, 946−950.
22. Fenn, T. D., Ringe, D., and Petsko, G. A. (2003) POVScript+: a program for model and data visualization using persistence of vision ray-tracing, *J. Appl. Crystallogr. 36*, 944−947.
23. DeLano, W. (2002) The PyMOL User's Manual, DeLano Scientific, San Carlos, CA.
24. Lanzetta, P. A., Alvarez, L. J., Reinach, P. S., and Candia, O. A. (1979) An improved assay for nanomole amounts of inorganic phosphate, *Anal. Biochem. 100*, 95−97.
25. Bradford, M. M. (1976) A rapid and sensitive method for the quantitation of microgram quantities of protein utilizing the principle of protein-dye binding, *Anal. Biochem. 72*, 248−254.
26. Kabsch, W., and Sander, C. (1983) Dictionary of protein secondary structure: pattern recognition of hydrogen-bonded and geometrical features, *Biopolymers 22*, 2577−2637.
27. Vincent, F., Yates, D., Garman, E., Davies, G. J., and Brannigan, J. A. (2004) The three-dimensional structure of the *N*-acetylglucosamine-6-phosphate deacetylase, NagA, from *Bacillus subtilis*: a member of the urease superfamily, *J. Biol. Chem. 279*, 2809−2816.
28. Holm, L., and Sander, C. (1993) Protein structure comparison by alignment of distance matrices, *J. Mol. Biol. 233*, 123−138.
29. Ireton, G. C., McDermott, G., Black, M. E., and Stoddard, B. L. (2002) The structure of *Escherichia coli* cytosine deaminase, *J. Mol. Biol. 315*, 687−697.
30. Hall, R. S., Brown, S., Fedorov, A. A., Fedorov, E. V., Xu, C., Babbitt, P. C., Almo, S. C., and Raushel, F. M. (2007) Structural Diversity within the Mononuclear and Binuclear Active Sites of *N*-Acetyl-D-glucosamine-6-phosphate Deacetylase, *Biochemistry 46*, 7953−7962.
31. Jozic, D., Kaiser, J. T., Huber, R., Bode, W., and Maskos, K. (2003) X-ray structure of isoaspartyl dipeptidase from *E. coli*: a dinuclear zinc peptidase evolved from amidohydrolases, *J. Mol. Biol. 332*, 243−256.
32. Aubert, S. D., Li, Y., and Raushel, F. M. (2004) Mechanism for the hydrolysis of organophosphates by the bacterial phosphotriesterase, *Biochemistry 43*, 5707−5715.
33. Thoden, J. B., Phillips, G. N., Jr., Neal, T. M., Raushel, F. M., and Holden, H. M. (2001) Molecular structure of dihydroorotase: a paradigm for catalysis through the use of a binuclear metal center, *Biochemistry 40*, 6989−6997.
34. Liaw, S. H., Chen, S. J., Ko, T. P., Hsu, C. S., Chen, C. J., Wang, A. H., and Tsai, Y. C. (2003) Crystal structure of D-aminoacylase from *Alcaligenes faecalis* DA1. A novel subset of amidohydrolases and insights into the enzyme mechanism, *J. Biol. Chem. 278*, 4957−4962.
35. Kawano, S., Nakashima, T., Kakuta, Y., Tanaka, I., and Kimura, M. (2006) Crystal structure of protein Ph1481p in complex with protein Ph1877p of archaeal RNase P from *Pyrococcus horikoshii* OT3: implication of dimer formation of the holoenzyme, *J. Mol. Biol. 357*, 583−591.
36. Wexler, M., Sargent, F., Jack, R. L., Stanley, N. R., Bogsch, E. G., Robinson, C., Berks, B. C., and Palmer, T. (2000) TatD is a cytoplasmic protein with DNase activity. No requirement for TatD family proteins in sec-independent protein export, *J. Biol. Chem. 275*, 16717−16722.
37. Yu, Y., Liang, Y. H., Brostromer, E., Quan, J. M., Panjikar, S., Dong, Y. H., and Su, X. D. (2006) A catalytic mechanism revealed by the crystal structures of the imidazolonepropionase from *Bacillus subtilis*, *J. Biol. Chem. 281*, 36929−36936.
38. Ferreira, F. M., Mendoza-Hernandez, G., Castaneda-Bueno, M., Aparicio, R., Fischer, H., Calcagno, M. L., and Oliva, G. (2006) Structural analysis of *N*-acetylglucosamine-6-phosphate deacetylase apoenzyme from *Escherichia coli*, *J. Mol. Biol. 359*, 308−321.
39. Jabri, E., Carr, M. B., Hausinger, R. P., and Karplus, P. A. (1995) The crystal structure of urease from *Klebsiella aerogenes*, *Science 268*, 998−1004.
40. Benini, S., Rypniewski, W. R., Wilson, K. S., Miletti, S., Ciurli, S., and Mangani, S. (1999) A new proposal for urease mechanism based on the crystal structures of the native and inhibited enzyme from *Bacillus pasteurii*: why urea hydrolysis costs two nickels, *Structure 7*, 205−216.
41. Smoukov, S. K., Quaroni, L., Wang, X., Doan, P. E., Hoffman, B. M., and Que, L., Jr. (2002) Electron-nuclear double resonance spectroscopic evidence for a hydroxo-bridge nucleophile involved in catalysis by a dinuclear hydrolase, *J. Am. Chem. Soc. 124*, 2595−2603.
42. Twitchett, M. B., and Sykes, A. G. (1999) Structure, Properties and Reactivity of the $Fe^{II}Fe^{III}$ and $Zn^{II}Fe^{III}$ Purple Acid Phosphatases, *Eur. J. Inorg. Chem. 1999*, 2105−2115.
43. Schenk, G., Gahan, L. R., Carrington, L. E., Mitic, N., Valizadeh, M., Hamilton, S. E., de Jersey, J., and Guddat, L. W. (2005) Phosphate forms an unusual tripodal complex with the Fe-Mn center of sweet potato purple acid phosphatase, *Proc. Natl. Acad. Sci. U.S.A. 102*, 273−278.
44. Ahn, S., Milner, A. J., Futterer, K., Konopka, M., Ilias, M., Young, T. W., and White, S. A. (2001) The "open" and "closed" structures of the type-C inorganic pyrophosphatases from *Bacillus subtilis* and *Streptococcus gordonii*, *J. Mol. Biol. 313*, 797−811.
45. Heikinheimo, P., Lehtonen, J., Baykov, A., Lahti, R., Cooperman, B. S., and Goldman, A. (1996) The structural basis for pyrophosphatase catalysis, *Structure 4*, 1491−1508.
46. Fabrichniy, I. P., Lehtio, L., Tammenkoski, M., Zyryanov, A. B., Oksanen, E., Baykov, A. A., Lahti, R., and Goldman, A. (2007) A trimetal site and substrate distortion in a family II inorganic pyrophosphatase, *J. Biol. Chem. 282*, 1422−1431.
47. Brooks, B. R., Bruccoleri, R. E., Olafson, B. D., States, D. J., Swaminathan, S., and Karplus, M. (1983) CHARMM: a program for macromolecular energy, minimization, and dynamics calculations, *J. Comput. Chem. 4*, 187−217.
48. Harutyunyan, E. H., Kuranova, I. P., Vainshtein, B. K., Hohne, W. E., Lamzin, V. S., Dauter, Z., Teplyakov, A. V., and Wilson, K. S. (1996) X-ray structure of yeast inorganic pyrophosphatase complexed with manganese and phosphate, *Eur. J. Biochem. 239*, 220−228.
49. Laskowski, R. A., MacArthur, M. W., Moss, D. S., and Thornton, J. M. (1993) PROCHECK: a program to check the stereochemical quality of protein structures, *J. Appl. Crystallogr. 26*, 283−291.

BI701204R